






## Article

# Synthesis and Characterization of N and Fe-Doped TiO<sub>2</sub> Nanoparticles for 2,4-Dimethylaniline Mineralization

Emerson Faustino <sup>1,2,†</sup>, Thalita Ferreira da Silva <sup>1,†</sup>, Rebeca Fabbro Cunha <sup>1</sup>, Diego Roberto Vieira Guelfi <sup>1</sup>, Priscila Sabioni Cavalheri <sup>1,3</sup>, Silvio César de Oliveira <sup>1</sup>, Anderson Rodrigues Lima Caires <sup>4</sup>, Gleison Antonio Casagrande <sup>1</sup>, Rodrigo Pereira Cavalcante <sup>1,5,\*</sup> and Amilcar Machulek Junior <sup>1,\*</sup>

<sup>1</sup> Institute of Chemistry, Federal University of Mato Grosso do Sul (UFMS), Av. Senador Filinto Muller, 1555, CP 549, Campo Grande 79074-460, MS, Brazil; emerson.faustino@ifro.edu.br (E.F.); thalita.quim@gmail.com (T.F.d.S.); rebecafabbro@hotmail.com (R.F.C.); diegoguelfi@outlook.com (D.R.V.G.); priscilasabioni@hotmail.com (P.S.C.); scolive@gmail.com (S.C.d.O.); gleisoncasag@gmail.com (G.A.C.)

<sup>2</sup> Federal Institute of Education, Science and Technology of Rondônia, Rodovia RO-257, s/n—Zona Rural, Ariquemes 76870-000, RO, Brazil

<sup>3</sup> Department of Sanitary and Environmental Engineering, Dom Bosco Catholic University, Campo Grande 79117-900, MS, Brazil

<sup>4</sup> Optics and Photonics Group, Institute of Physics, Federal University of Mato Grosso do Sul (UFMS), Campo Grande 79070-900, MS, Brazil; anderson.caires@ufms.br

<sup>5</sup> School of Technology, University of Campinas—UNICAMP, Paschoal Marmo, 1888, Limeira 13484-332, SP, Brazil

\* Correspondence: rodrigoquimica14203@yahoo.com.br (R.P.C.); machulekjr@gmail.com (A.M.J.)

† These authors contributed equally to this work.



**Citation:** Faustino, E.; da Silva, T.F.; Cunha, R.F.; Guelfi, D.R.V.; Cavalheri, P.S.; de Oliveira, S.C.; Caires, A.R.L.; Casagrande, G.A.; Cavalcante, R.P.; Junior, A.M. Synthesis and Characterization of N and Fe-Doped TiO<sub>2</sub> Nanoparticles for 2,4-Dimethylaniline Mineralization. *Nanomaterials* **2022**, *12*, 2538. <https://doi.org/10.3390/nano12152538>

Academic Editor: Vincenzo Vaiano

Received: 2 July 2022

Accepted: 22 July 2022

Published: 24 July 2022

**Publisher's Note:** MDPI stays neutral with regard to jurisdictional claims in published maps and institutional affiliations.



**Copyright:** © 2022 by the authors. Licensee MDPI, Basel, Switzerland. This article is an open access article distributed under the terms and conditions of the Creative Commons Attribution (CC BY) license (<https://creativecommons.org/licenses/by/4.0/>).

**Abstract:** The present study aimed to evaluate the feasibility of developing low-cost N- and Fe-doped TiO<sub>2</sub> photocatalysts for investigating the mineralization of 2,4-dimethylaniline (2,4-DMA). With a single anatase phase, the photocatalysts showed high thermal stability with mass losses of less than 2%. The predominant oxidative state is Ti<sup>4+</sup>, but there is presence of Ti<sup>3+</sup> associated with oxygen vacancies. In materials with N, doping was interstitial in the NH<sub>3</sub>/NH<sup>4+</sup> form and for doping with Fe, there was a presence of Fe-Ti bonds (indicating substitutional occupations). With an improved band gap energy from 3.16 eV to 2.82 eV the photoactivity of the photocatalysts was validated with an 18 W UVA lamp (340–415 nm) with a flux of 8.23 × 10<sup>−6</sup> Einstein s<sup>−1</sup>. With a size of only 14.45 nm and a surface area of 84.73 m<sup>2</sup> g<sup>−1</sup>, the photocatalyst doped with 0.0125% Fe mineralized 92% of the 2,4-DMA in just 180 min. While the 3% N photocatalyst with 12.27 nm had similar performance at only 360 min. Factors such as high surface area, mesoporous structure and improved E<sub>bg</sub>, and absence of Fe peak in XPS analysis indicate that doping with 0.0125% Fe caused a modification in TiO<sub>2</sub> structure.

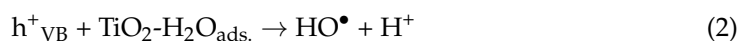
**Keywords:** 2,4-dimethylaniline; N-Fe-doped TiO<sub>2</sub>; characterization

## 1. Introduction

2,4-Dimethylaniline (2,4-DMA, also called 2,4-Xylidine, C.A.S. No. 95-68-1) is an aromatic amine used as a precursor for some textile dyes and veterinary drugs [1,2]. Considered a persistent contaminant, 2,4-DMA has already been detected in industrial effluents and groundwater. For example, 2,4-DMA was detected in textile industry wastewater even after anaerobic treatment processes [3]. Toxicologically, 2,4-DMA has been classified as a group 3 carcinogen and has adverse effects on the aquatic ecosystem [4]. Furthermore, 2,4-DMA is a model compound used in degradation studies because its oxidation produces intermediates that facilitate mechanistic studies [5,6].

Persistent contaminants exhibit chemical and biological resistance to mineralization through traditional water treatment methods. Therefore, the search for innovative treatment technologies has increased. Advanced oxidation processes (AOPs) are an alternative to

completely mineralizing for numerous contaminants, as it is not a selective process [7]. AOPs are able to remove various types of pollutants from attacks by reactive oxygen species (ROS) generated in the system [8–16]. Heterogeneous photocatalysis (PC) are AOPs that involves the activation of a photocatalyst by light irradiation. Under specific conditions, photogenerated charge carriers ( $e^-_{CB}$  and  $h^+_{VB}$ ) undergo interfacial transfer and promote redox reactions with adsorbed molecular oxygen, water molecules, and hydroxide ions, producing various types of ROS such as superoxide, hydrogen peroxide, and hydroxyl radicals ( $HO^\bullet$ ) [13,17]. Many semiconductors, such as  $TiO_2$  [18],  $WO_3$  [14],  $ZnO$  [19], and  $BiVO_4$  [20], have been used to photodegrade emerging contaminants.  $TiO_2$  is the most investigated photocatalyst due to its low toxicity, low cost, chemical stability over a wide pH range, thermal stability, minimizing  $e^-_{CB}/h^+_{VB}$  pair recombination, and the band gap energy ( $E_{bg}$ ) being able to oxidize water molecules generating  $HO^\bullet$  radicals. The principle of PC involves the activation of a semiconductor by solar or artificial irradiation, Equation (1). Photons absorbed with energy greater than the  $E_{bg}$  promote an electron from the valence band to the conduction band with the simultaneous generation of a hole ( $h^+_{VB}$ ) in the valence band. The adsorbed water ( $H_2O_{ads.}$ ) is oxidized in the  $h^+_{VB}$  generating  $HO^\bullet$ , which can subsequently oxidize the organic contaminant (R), Equations (2) and (3). Or the R can be oxidized directly in the  $h^+_{VB}$ , Equation (4).



$TiO_2$  has a high  $E_{bg}$  (3.2 eV for anatase) and is excited only by ultraviolet light irradiation ( $\lambda < 385$  nm) [21]. The photocatalytic activity of  $TiO_2$  can be improved by doping or modifying its crystalline structure in order to increase the optical absorption of radiation in the visible range and decrease the rate of recombination of photogenerated charges [22]. Light absorption of  $TiO_2$  in the visible region can be improved via metal- [23–25] or non-metal-doping [18,26,27]. Several approaches for the synthesis of  $TiO_2$  have been reported, such as sol-gel, hydrothermal, solvothermal, and spray pyrolysis [28–31]. Among them, the sol-gel method has been considered a good solution to produce nanomaterials, presenting advantages such as homogeneity, ease and flexibility in introducing doping at high concentrations, simple synthesis process, and providing nanomaterials with high purity. During sol-gel preparation, a  $TiO_2$  sol or gel is formed by precipitation through the hydrolysis and condensation of a titanium alkoxide [18]. Jadhav et al. synthesized N-doped  $TiO_2$  doped with 25% N using urea as a precursor. The material synthesized by them degraded 70% of the methylene blue in 180 min of the experiment under visible light [32]. Synthesis using ammonium salt as precursor has also been reported and its photocatalytic activity showed a 90% removal in 40 min of rhodamine B [33]. Yalçın et al. synthesized Fe-doped photocatalysts and tested the photoactivity on 4-nitrophenol degradation degrading 80% in 120 min [34].

In this work, we synthesized and characterized N-, Fe-, and N-Fe-doped  $TiO_2$  nanoparticles via sol-gel. Furthermore, we evaluated the photocatalytic activities of  $TiO_2$  NPs through 2,4-DMA mineralization. This research provides new results on the influence of nitrogen and iron on  $TiO_2$  on 2,4-DMA mineralization. It is worth mentioning that, to the best of our knowledge, no studies were reported involving the photocatalysis process with N-, Fe- doped  $TiO_2$  for the mineralization of 2,4-DMA, with good results of mineralization rates in 6 h in an unprecedented manner.

## 2. Materials and Methods

### 2.1. Synthesis of Photocatalysts

The synthesis of photocatalysts via sol-gel followed the procedure described below [18,35]. A volume of 19.10 mL of titanium IV isopropoxide (97%, Sigma Aldrich, St. Louis, MO, USA) and 16.10 mL of glacial acetic acid (99.7%, Alphatec, Carlsbad, CA, USA) was added to a beaker and left under magnetic stirring. After homogenization, 19.10 mL of 2-propanol (99.6%, Merck, Kenilworth, NJ, USA) was added and left under stirring for 60 min. Thereupon, 30 mL of deionized water (resistivity > 18 MΩ cm obtained from Gehaka DG500 UF system, São Paulo, SP, Brazil) acidified with 1 mL of nitric acid (65.0%, Vetec, Duque de Caxias, RJ, Brazil) was added dropwise to the above solution. At the end of the addition, the solution was stirred for another 120 min. Finally, the resulting product was maintained at 40 °C for about 48 h for gel formation. The gel was dried in an oven at 100 °C for 24 h. The product has been macerated and placed in a muffle furnace at 450 °C for 4 h.

The synthesis of TiO<sub>2</sub> doped with N, Fe, and N-Fe followed the same procedure described above, but there was the addition of ammonium hydroxide (25%, Merck, Kenilworth, NJ, USA) as a source of N and iron III nitrate (98%, Vetec) as a precursor of Fe. N-doped TiO<sub>2</sub> were prepared in the different weight content of nitrogen (%): 1.0, 2.0, 3.0, 4.0, 5.0, 6.0, 7.0, and 9.0 (*w/w*). Fe-doped TiO<sub>2</sub> were prepared in the different weight content of iron (%): 0.0125, 0.025, 0.05, 0.1, 0.25, and 1.0 (*w/w*). N-Fe co-doped TiO<sub>2</sub> were prepared by fixing 0.025% Fe and varying only N by 2, 3, and 4% (*w/w*). These concentrations of N and Fe were chosen based on previous work [18,35]. The effects of the presence of N and Fe on the physical and chemical properties of photocatalyst particles were investigated by increasing or decreasing the photocatalytic response in 2,4-DMA mineralization. Figure 1 presents a schematic representation showing the steps of the synthesis.

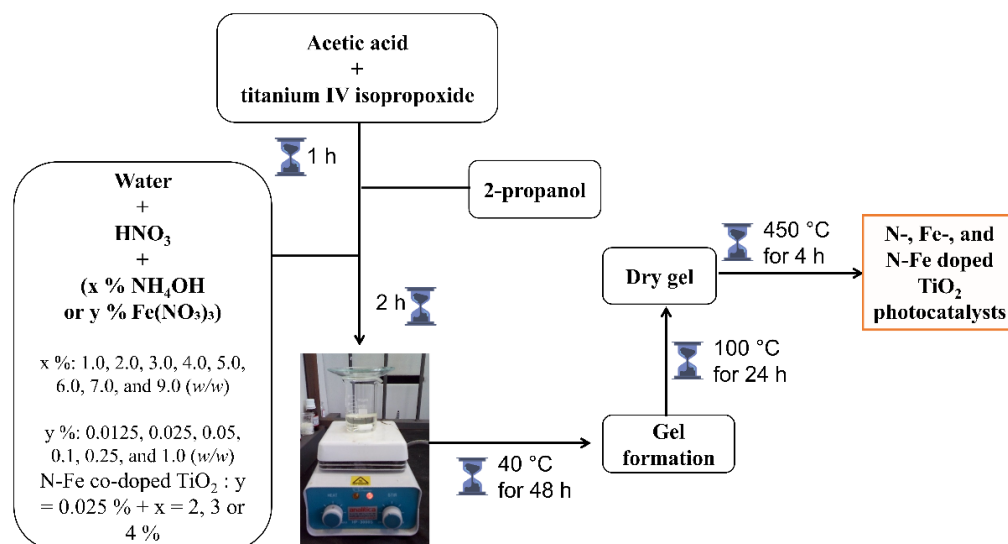


**Figure 1.** Representative scheme showing the steps of the catalyst synthesis process.

### 2.2. Photocatalysts Characterization

The nanoparticles synthesized from pure TiO<sub>2</sub>, N, and Fe-doped TiO<sub>2</sub> are characterized by thermogravimetric (TG) and differential thermogravimetric (DTG) curves recorded by the TA Instruments thermal analyzer-TGA Q50. Approximately 10 mg of each sample was used and the thermocurves are recorded in the range of room temperature to 850 °C in atmosphere of nitrogen (N<sub>2</sub>) gas. The crystalline structure of the synthesized pure TiO<sub>2</sub>, N, and Fe-doped TiO<sub>2</sub> nanoparticles is carried out by powder X-ray diffraction (XRD) technique employing LabX XRD-6100, Shimadzu. The XRD analysis is done in the 2θ range of 10° and 70° using Co Kα radiation of wavelength 17,889 Å. Fourier transform infrared spectroscopy (FTIR) analysis of the samples was performed with a PerkinElmer FTIR

spectrophotometer, Frontier model. The samples were prepared by the KBr pellet pressing method, at room temperature and in the region of 4000–450  $\text{cm}^{-1}$ . The morphological of the materials was studied by Scanning Electron Microscopy (SEM) in a JSM-6380LV JEOL microscope and Transmission Electron Microscopy (TEM) in a model JEM 2100 LaB<sub>6</sub> JEOL microscope. Using the ImageJ software and TEM images, the diameter of the particles in the different samples was measured [18]. Diffuse UV-visible reflectance spectroscopy (DRS) analyzes were performed on the samples using a PerkinElmer Lambda 650 UV/Vis/NIR spectrophotometer operating in the range of 200–800 nm. From the DRS studies, a graph of the modified Kubelka-Munk function  $[F(R) \times hv]^{1/2}$  versus absorbed light energy was constructed for indirect band gap energy ( $E_{bg}$ ) calculations. The surface area and pore size distribution of the samples were calculated by the Brunauer-Emmett-Teller (BET) method using the ASAP 2010, Micromeristic surface area analyzer. X-ray photoelectron spectroscopy (XPS) measurements were performed on a EA125 Sphera spectrometer. The elemental composition of the samples was determined by X-ray photoelectron spectroscopy (XPS). The analyzes were performed on an Omicron, model EA125 Sphera equipped with a hemispherical electron analyzer. All measurements were performed in an ultra-high vacuum (UHV) chamber with pressure between  $10^{-8}$  and  $10^{-12}$  mbar. The C1s peak of carbon contamination at 284.60 eV was used as a binding energy reference.

### 2.3. Photocatalytic Mineralization

The photocatalytic activity of the synthesized materials was tested for the mineralization of 2,4-DMA. In a typical procedure, 350 mL ( $0.1 \text{ mmol L}^{-1}$ ) of 2,4-DMA solution and 175 mg of photocatalyst were transferred to a glass reactor. The suspension was kept under constant stirring in the dark for 30 min, ensuring the adsorption-desorption equilibrium of the test molecule. A UVA lamp (18 W, DULUX L-OSRAM,  $\lambda = 340\text{--}415 \text{ nm}$  and  $8.23 \times 10^{-6} \text{ Einstein s}^{-1}$ ) was used as irradiation. After the adsorption-desorption equilibrium was established, the lamp was turned on, and 4 mL aliquots were collected at different times. The mineralization was followed by the total organic carbon (TOC) analysis using a Shimadzu TOC VCPN analyzer. The calibration accuracy values with LOQ =  $0.180 \text{ mg L}^{-1}$  and LOD =  $0.053 \text{ mg L}^{-1}$  were obtained. The reuse experiments lasted 180 min and various aliquots were collected and analyzed by TOC. The photocatalyst used was collected by vacuum filtration, washed with deionized water (resistivity > 18 M $\Omega$  cm obtained from Gehaka DG500 UF system, São Paulo, Brazil) and dried in an oven at 80 °C (Medicate, MD 1.2). The reuse experiment cycle was repeated three times.

Apparent pseudo-first order kinetic constants ( $k_{2,4\text{-DMA}}$ ) (Equation (5)) to 2,4-DMA were calculated according to the following:

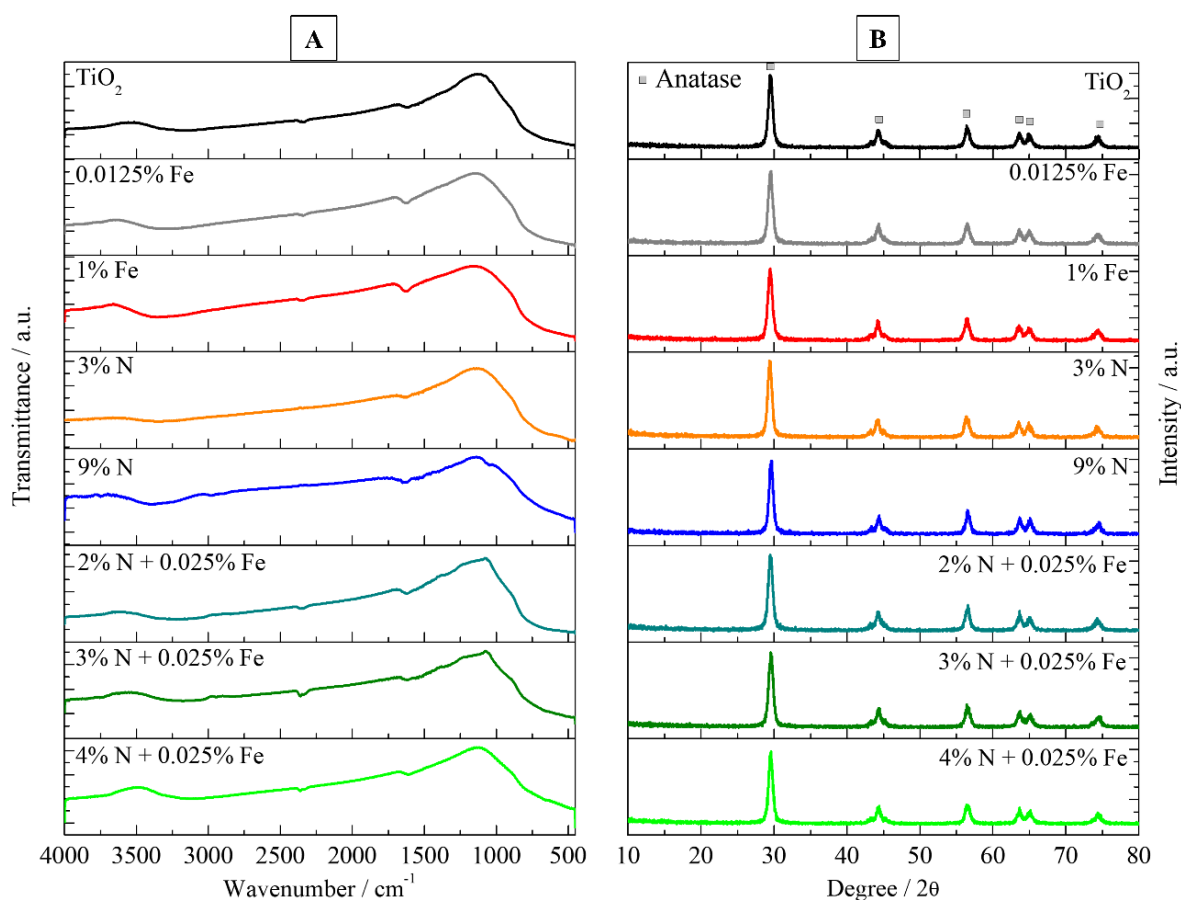
$$k_{2,4\text{-DMA}} = \frac{\ln \frac{[\text{TOC}]_0}{[\text{TOC}]_t}}{t} \quad (5)$$

## 3. Results and Discussion

### 3.1. Characterization of N-, Fe-, and N-Fe Doped TiO<sub>2</sub> Photocatalysts

Figure S1 (see Supplementary Material) shows the results of the TG and DTG analysis for the synthesized N-, Fe-, and N-Fe doped TiO<sub>2</sub> nanoparticles. It can be seen in Figure S1A, that the synthesized materials have a high thermal stability independent of doping. The mass losses were less than 3%, which is consistent with previous works [25,36,37]. In the DTG curves (Figure S1B), an endothermic event before 100 °C can be seen and is associated with evaporation of adsorbed water and/or decomposition of residual organic matter.

Some characteristic peaks of TiO<sub>2</sub>-based photocatalysts can be seen in Figure 2A. The bands at 700  $\text{cm}^{-1}$  are typical of the Ti-O and Ti-O-Ti bonds present in TiO<sub>2</sub>. The bands at 1650  $\text{cm}^{-1}$  and 3200  $\text{cm}^{-1}$  are associated with the O-H vibrational modes of adsorbed water. The N-doped photocatalysts present bands close to 1500  $\text{cm}^{-1}$  and 3200  $\text{cm}^{-1}$ , referring to the vibration of the N-H group [32]. The vibrational bands of the Fe-O bond are in the range of 400 to 700  $\text{cm}^{-1}$ , but they were not observed due to the low concentration of iron used.



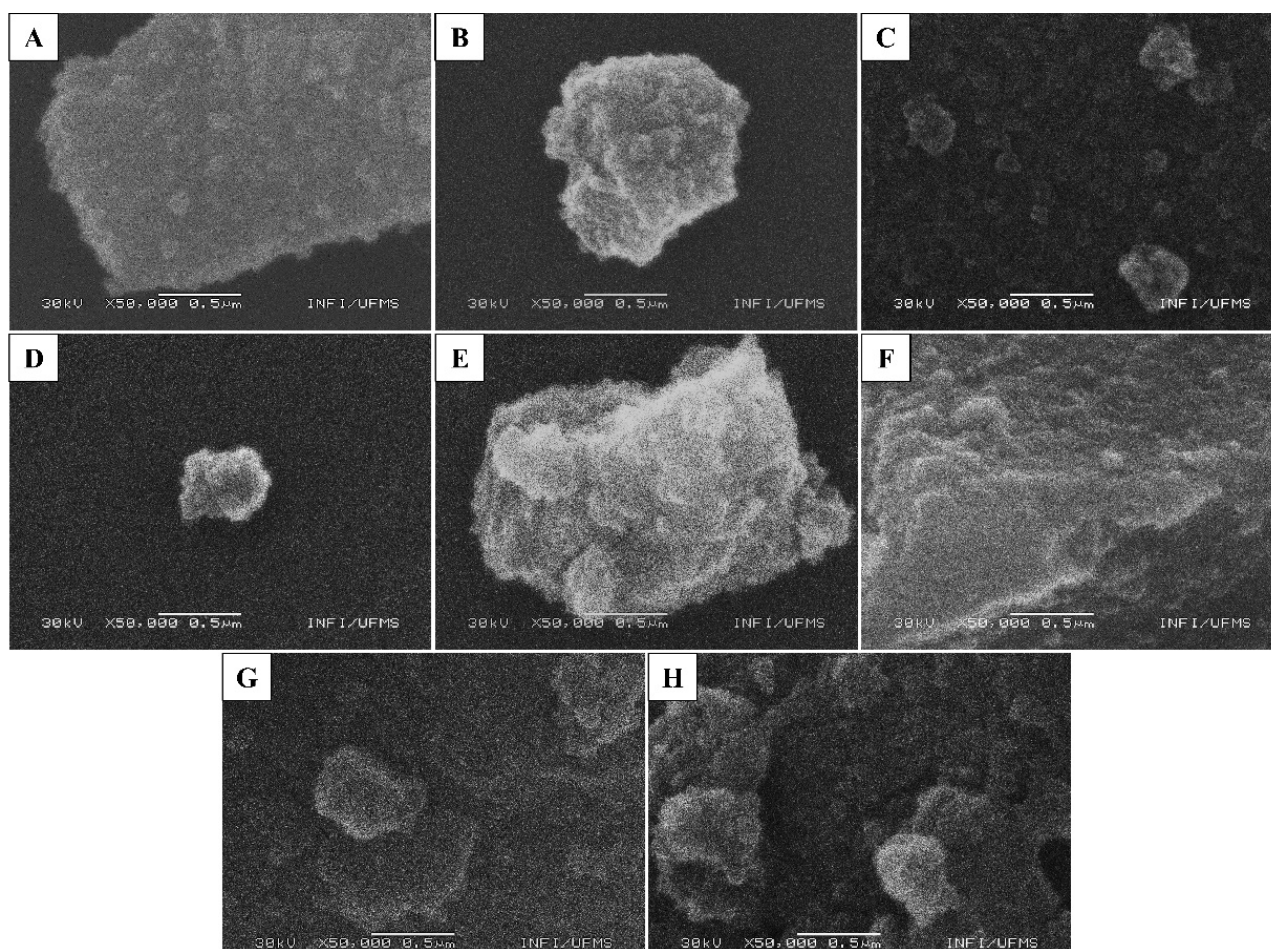
**Figure 2.** (A) FTIR spectra, and (B) X-ray diffraction patterns of N-, Fe-, and N-Fe doped TiO<sub>2</sub> photocatalysts.

Figure 2B shows XRD patterns for the investigated photocatalysts. The anatase phase peaks at 29.54° (101) and 44.14° (200) compared to ICDD Card no. 00–021–1272, are present in the samples. The peaks of the rutile phase are absent in the diffractograms. The calcination temperature (450 °C) does not promote the formation of this crystalline phase [38]. The other peaks at 56.36° (105), 63.50° (116), 64.96° (200), and 74.44° (2015) are also due to the anatase phase belonging to the tetragonal crystal system [13]. From the Rietveld refinement (see Figure S2 and Table S1 in the Supplementary Material) the special group I4<sub>1</sub>/amd (141) and a density of 3.90 g cm<sup>−3</sup> for TiO<sub>2</sub>, 0.125%Fe-TiO<sub>2</sub> and 3%N-TiO<sub>2</sub>. The presence of the anatase phase in the photocatalysts is consistent with the literature [25,39].

Obtaining the anatase phase is satisfactory, as it allows a more effective absorption of photons than the rutile phase of TiO<sub>2</sub>. The anatase phase of TiO<sub>2</sub> increases the photocatalytic performance compared to the rutile phase as it increases the redox power of the charge carriers and can enhance the adsorb of hydroxyl groups on its surface [40]. In the case of Fe doping, the absence of peaks at 31.07° corresponding to Fe<sub>3</sub>O<sub>4</sub> and 36.18° and 41.30° corresponding to FeTiO<sub>3</sub> in Figure 2B indicates that Fe<sup>3+</sup> cations did not react with TiO<sub>2</sub> [34,41]. The absence of these oxides is desirable because their presence reduces photocatalytic activity [34]. Therefore, substitutional doping of Fe<sup>3+</sup> occurred in the photocatalysts instead of interstitial doping.

The morphology and size of N-, Fe-, and N-Fe doped TiO<sub>2</sub> photocatalysts were investigated by SEM (Figure 3) and TEM (Figure 4). According to Figure 3A–G, the morphology of the synthesized oxides does not follow a defined pattern, presenting clusters in a slightly rounded shape on their surface. In some cases, the clusters are larger than

others, as seen in the A (pure), D (3% N), E (9% N), and F (2% N + 0.025% Fe) images in Figure 3.



**Figure 3.** SEM image of the surfaces of N-, Fe-, and N-Fe doped TiO<sub>2</sub> photocatalysts. (A) TiO<sub>2</sub> pure, (B) 0.0125% Fe, (C) 1% Fe, (D) 3% N, (E) 9% N, (F) 2% N + 0.025% Fe, (G) 3% N + 0.025% Fe, and (H) 4% N + 0.025% Fe.

Figure 4 shows the TEM micrographs and the particle diameter distribution histogram. The data show that the TiO<sub>2</sub> photocatalysts have an average particle diameter of 16.16 nm (Figure 4A), while 0.0125% Fe (Figure 4B) and 3% N (Figure 4C) have 14.45 nm and 12.27 nm, respectively. TiO<sub>2</sub> doping resulted in particle reduction, regardless of the dopant used.

N<sub>2</sub> adsorption-desorption isotherm at liquid nitrogen temperature was conducted to analyze the pore size and surface area of N-, Fe-, and N-Fe doped TiO<sub>2</sub> photocatalysts, as shown in Figure 5. BET surface areas ( $S_{\text{BET}}$ ), pore volume ( $V_p$ ) and pore diameters ( $D_p$ ) are shown in Table 1. The samples show surface areas of 78.67, 84.73, and 95.70 m<sup>2</sup> g<sup>-1</sup> for TiO<sub>2</sub>, 0.0125% Fe, and 3% N, respectively. In Figure 4, we clearly see that the samples are agglomerates formed by monodisperse primary particles, with sizes of 16.16, 14.45, and 12.27 nm for TiO<sub>2</sub>, 0.0125% Fe, and 3% N, respectively. Table 1 indicates that the nanoparticles are porous with mean pore diameters of 9.7 to 9.0 nm and narrow pore size distributions (Figure 5). Farhangi et al. reported that Fe doping could decrease TiO<sub>2</sub> crystallization and also slightly restrict TiO<sub>2</sub> crystallite growth [42]. The presence of N- and Fe- caused a decrease in the nanoparticle and an increase in its surface area. Large surface area and mesoporous structure are favorable characteristics for obtaining high photocatalytic activity.

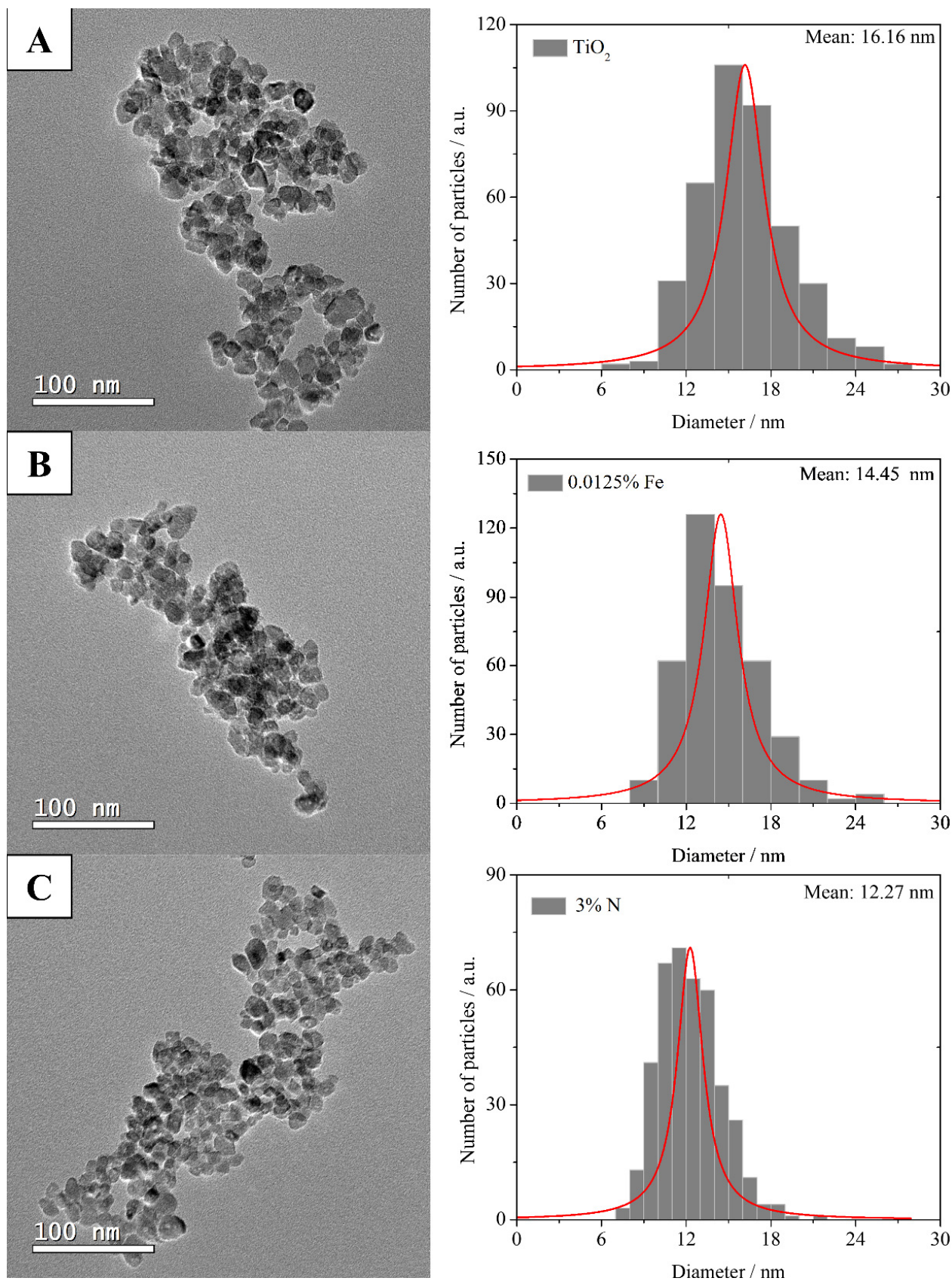
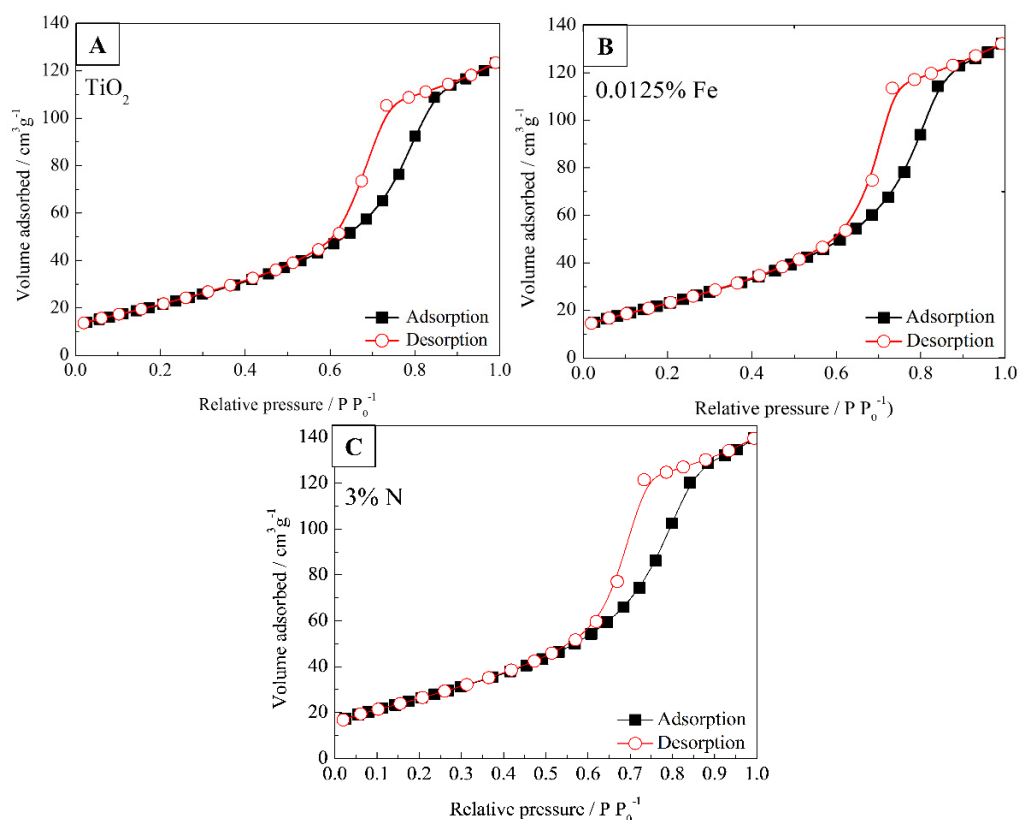


Figure 4. TEM images and their size distributions of particles (A)  $\text{TiO}_2$ , (B) 0.0125% Fe, and (C) 3% N.



**Figure 5.** Nitrogen adsorption-desorption isotherms of (A)  $\text{TiO}_2$ , (B) 0.0125% Fe, and (C) 3%N.

**Table 1.** BET surface areas ( $S_{\text{BET}}$ ), pore volume ( $V_p$ ), and pore diameters ( $D_p$ ) for the N-, Fe-, and N-Fe doped  $\text{TiO}_2$  photocatalysts.

Photocatalysts	$S_{\text{BET}}$ ( $\text{m}^2 \text{g}^{-1}$ )	$D_p$ (nm)	$V_p$ ( $\text{cm}^3 \text{g}^{-1}$ )
$\text{TiO}_2$	$78.67 \pm 1.50$	9.73	0.19
$\text{TiO}_2 + 0.0125\% \text{Fe}$	$84.73 \pm 1.47$	9.68	0.20
$\text{TiO}_2 + 3\% \text{N}$	$95.70 \pm 1.38$	9.04	0.22

The chemical composition and electronic states of the photocatalyst constituents: pure  $\text{TiO}_2$ , 0.0125% Fe and 3% N were investigated by XPS, as shown in Figure 6. According to the survey spectrum Ti, O, and C peaks are evident. For all samples can be observed the presence of peaks related to Ti 3p, Ti 3s, C 1s, Ti 2p, O 1s, and Ti 2s at around 26.0, 39.0, 286.0, 462.0, 533.0, and 566.0 eV, respectively. The origin of carbon is common in XPS analyses, resulting from the strong adsorption of a contaminating layer or hydrocarbon from the carbon strip of the instrument [35,43]. The chemical composition of photocatalysts is shown in Table 2. As seen in Figure 7A–C, two peaks at approximately 458.5 and 464.3 eV that correspond to typical  $\text{Ti}^{4+}$  2p<sub>3/2</sub> and  $\text{Ti}^{4+}$  2p<sub>1/2</sub>, are observed for all samples [34,44]. In Figure 7A–C, the Ti 2p<sub>3/2</sub> peak at 457.1 eV and the Ti 2p<sub>1/2</sub> peak at 462.8 eV correspond to the  $\text{Ti}^{3+}$  species [45]. The O 1s signals for all samples (Figure 7D–F) can be divided into two peaks at 529.8 and 531.0 eV, corresponding to Ti–O and surface –OH bonds, respectively [44]. For comparison purposes, the contribution of the peaks at 531.0 eV at 0.0125% Fe (24.9%) and 3%N (17.1%) is lower than that of  $\text{TiO}_2$  (42.0%), indicating fewer oxygen vacancies in the doped catalysts. Oxygen vacancies on the surface of the particle tend to promote more –OH bonds [46]. Metallic Fe signals were not observed at 710.7 eV for 2p<sub>3/2</sub> and 724.3 eV for 2p<sub>1/2</sub>, which indicates the absence of  $\text{Fe}_2\text{O}_3$  [34]. As the presence of metallic Fe was not detected, the iron cations probably occupied substitutional positions due to the similar radius of  $\text{Fe}^{3+}$  (0.64 Å) and  $\text{Ti}^{4+}$  (0.68 Å), forming a solid Fe–Ti solution during the sintering process (<1 at Fe%) [47]. The peak at 399.1 eV in Figure S3 refers to



the N 1s that are present in the 3% N sample, this peak is characteristic of interstitial N. Values above 400 eV can be assigned to groups  $\text{NO}_2^-$ ,  $\text{N}_2$  and  $\text{NH}_x$ . As shown by the results obtained from FTIR (Figure 2A) there are vibrations in the N-H group, so it can be said that the peak of N 1s is nitrogen in the  $\text{NH}_3/\text{NH}_4^+$  form. It is considered that nitrogen does not replace the oxygen atom in the crystal matrix, it was incorporated to form Ti-O-N bonds on the surface of the material [25,48].

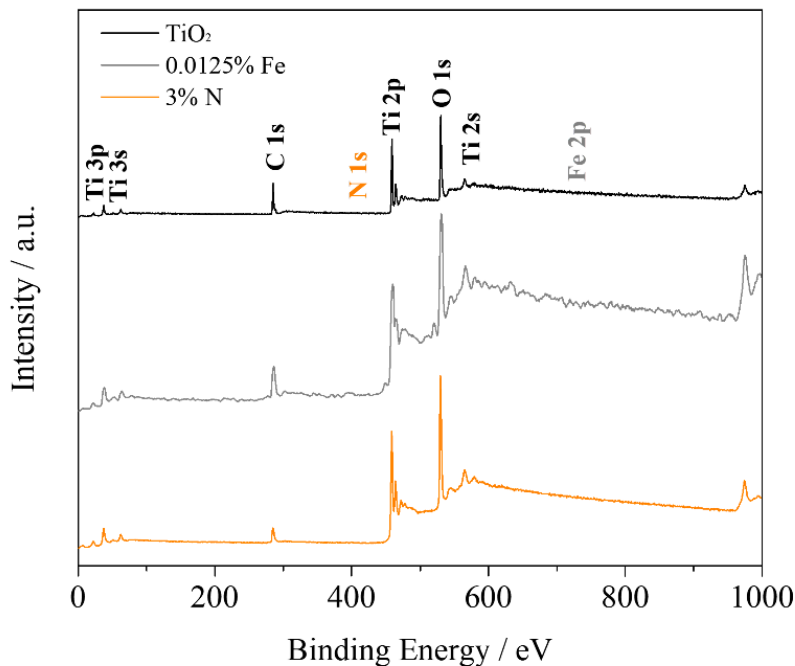


Figure 6. XPS spectra for the  $\text{TiO}_2$ , 0.0125% Fe, and 3%N samples.

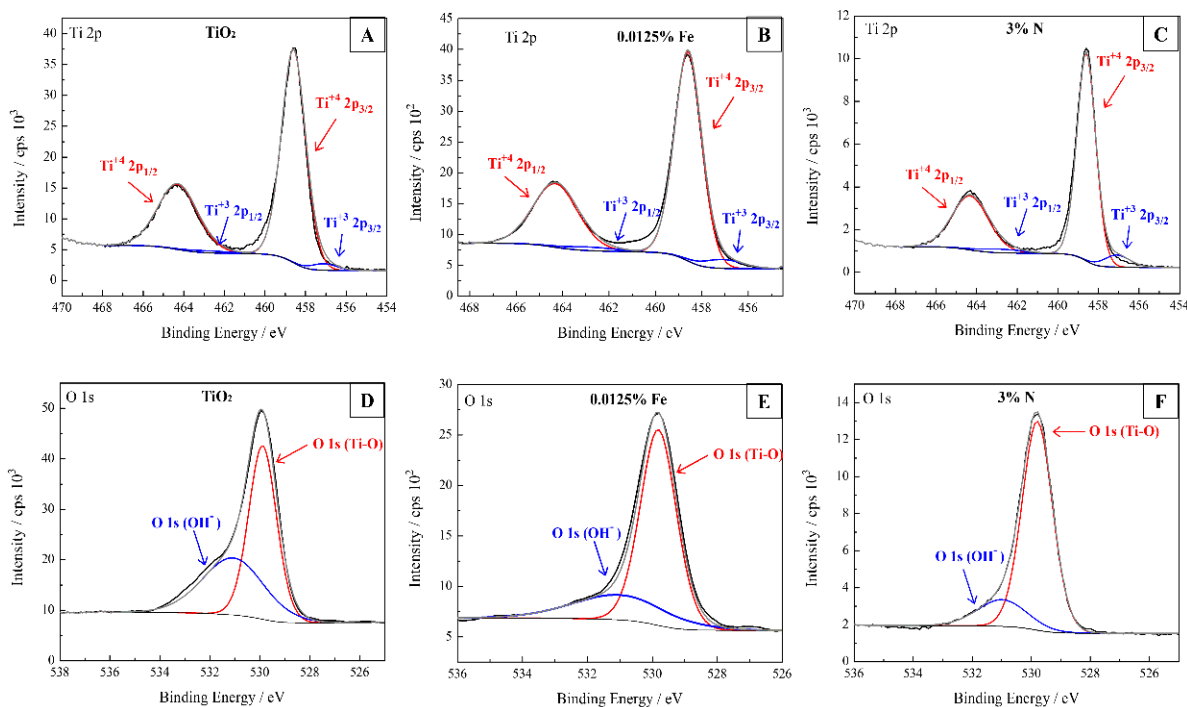
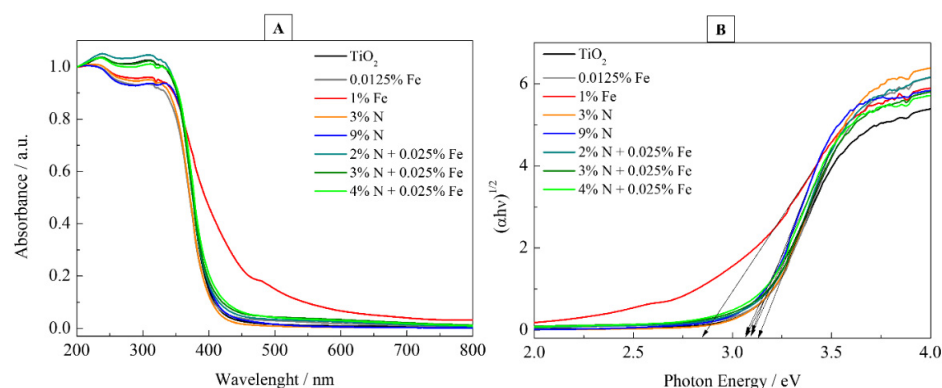


Figure 7. High-resolution XPS Ti 2p and O 1s spectra of  $\text{TiO}_2$  (A,D), 0.0125% Fe (B,E) and 3% N (C,F).

**Table 2.** Binding energies/eV and contribution of the high-resolution spectra of Ti 2p present in the photocatalysts. Values are obtained from high-resolution XPS spectra in Figure 6.

Photocatalysts	Composition Ti	Binding Energies/eV Ti 2p <sub>1/2</sub>	Binding Energies/eV Ti 2p <sub>3/2</sub>	Contribution/%
TiO <sub>2</sub>	Ti <sup>4+</sup>	464.30	458.58	96.84
	Ti <sup>3+</sup>	462.80	457.08	03.16
0.0125% Fe	Ti <sup>4+</sup>	464.30	458.58	94.20
	Ti <sup>3+</sup>	462.80	457.08	05.80
3% N	Ti <sup>4+</sup>	464.31	458.59	97.64
	Ti <sup>3+</sup>	462.81	457.09	07.38

The UV-visible absorption spectra of N-, Fe-, and N-Fe doped TiO<sub>2</sub> photocatalysts are presented in Figure 8. The absorption spectra in Figure 8A shows intense absorption in the region of 300 to 450 nm, resulting from the intrinsic band gap of TiO<sub>2</sub>. The 1% Fe photocatalyst showed improved absorption in the visible range (in the 400 to 700 nm) when compared to other doped photocatalysts. The  $E_{bg}$  (Figure 8B) of the samples was estimated using Tauc's formula and their values are found in Table 3. Pure TiO<sub>2</sub> had an  $E_{bg}$  of 3.16 eV, a value close to that reported in the literature [18]. The  $E_{bg}$  values for N-doped catalysts showed a small difference in relation to pure TiO<sub>2</sub>. The likely reason behind the decrease in the  $E_{bg}$  is that the nitrogen inside the TiO<sub>2</sub> doped material replaces the Ti ions inside the material [32], as seen in Figure 8. For the Fe-doped photocatalysts, a gradual decrease is observed with increasing Fe concentration. This effect may be associated with the new energy levels introduced in the TiO<sub>2</sub> band gap caused by Fe<sup>3+</sup> and Fe<sup>2+</sup> ions. The 1% Fe photocatalyst presented an  $E_{bg}$  of 2.82 eV. This value is 0.34 eV lower than the band gap of pure TiO<sub>2</sub> anatase nanoparticles (3.16 eV), which can be caused by Ti<sup>3+</sup> sites (vacancies of oxygen) [49] as a role of the intermediate trap state formed in the calcination process. Barkhade and Banerjee also detected a decrease in  $E_{bg}$  from 3.4 eV for pure TiO<sub>2</sub> to 2.5 eV for a TiO<sub>2</sub> sample doped with 1.0% Fe (mol %). They attributed the decrease to the insertion of Fe<sup>3+</sup> ions into the TiO<sub>2</sub> lattice in which conduction band overlap occurred due to the Ti (d-orbital) of TiO<sub>2</sub> and the metal (d-orbital) orbital of Fe<sup>3+</sup> ions. Furthermore, the doping of Fe<sup>3+</sup> ions induces the formation of new electronic states (Fe<sup>4+</sup> and Fe<sup>2+</sup>) that span across the TiO<sub>2</sub> band gap [50].

**Figure 8.** (A) UV-Vis absorbance spectra for the synthesized photocatalysts. (B) Tauc plots of photocatalysts with different % N and Fe.

The photocatalytic efficiency of a catalyst depends on some aspects such as light absorption, charge separation and types of catalysts. The fundamental reaction in photocatalysis occurs with the absorption of light [51], which leads to charge separation and formation of active species, as shown in Equations (1)–(4). The charge carriers generated can separate and then recombine. But they can also migrate to the surface of the catalyst and recombine in surface traps or undergo interfacial electron transfer with the reduced species. The recombination kinetics is related to the presence of impurities in the bulk and

recombination centers on the catalyst surface. Therefore, the quantum yield of a doped catalyst is often lower than that of the related undoped material. However, light capture plays an important role in determining the rate of degradation of organic molecules. Consequently, here the improved light-gathering capacity of N-, Fe- and N-Fe-doped TiO<sub>2</sub> photocatalysts would be beneficial to increase their photocatalytic activity.

**Table 3.** Band gap energy values for all photocatalysts.

Photocatalysts	E <sub>bg</sub> /eV
TiO <sub>2</sub>	3.16
TiO <sub>2</sub> + 0.0125%Fe	3.08
TiO <sub>2</sub> + 1%Fe	2.82
TiO <sub>2</sub> + 3%N	3.14
TiO <sub>2</sub> + 9%N	3.07
3% N + 0.025% Fe	3.05
4% N + 0.025% Fe	3.06

### 3.2. Photocatalytic Activity

The photocatalytic activity of N-, Fe-, and N-Fe doped TiO<sub>2</sub> was measured using a 2,4-DMA solution under UVA light. The effects of nitrogen content (1, 2, 3, 4, 5, 6, 7, 9%), iron (0.0125, 0.025, 0.05, 0.1, 0.25, and 1%) and N-Fe co-doping (3% N +0.025% Fe, and 4% N + 0.025% Fe) were investigated by TOC (Total Organic Carbon) with their respective pseudo-first-order constants ( $k_{2,4\text{-DMA}}$ ).

Figure 9A shows the relationship between 2,4-DMA mineralization and irradiation time for each x% N photocatalyst during PC, and in Figure 9B their respective  $k_{2,4\text{-DMA}}$ . In 360 min of the experiment, the 3% N and 4% N photocatalysts mineralized 100% and presented a  $k_{2,4\text{-DMA}}$  of 0.007 min<sup>-1</sup> and 0.006 min<sup>-1</sup>, respectively. Furthermore, the values of  $k_{2,4\text{-DMA}}$  were 1.8 and 1.5 times higher than mineralization with pure TiO<sub>2</sub> (Table 4). Analyzing the experiment time at 240 min, we see that increasing the percentage of nitrogen up to 3% (*w/w*) promotes an increase in mineralization.

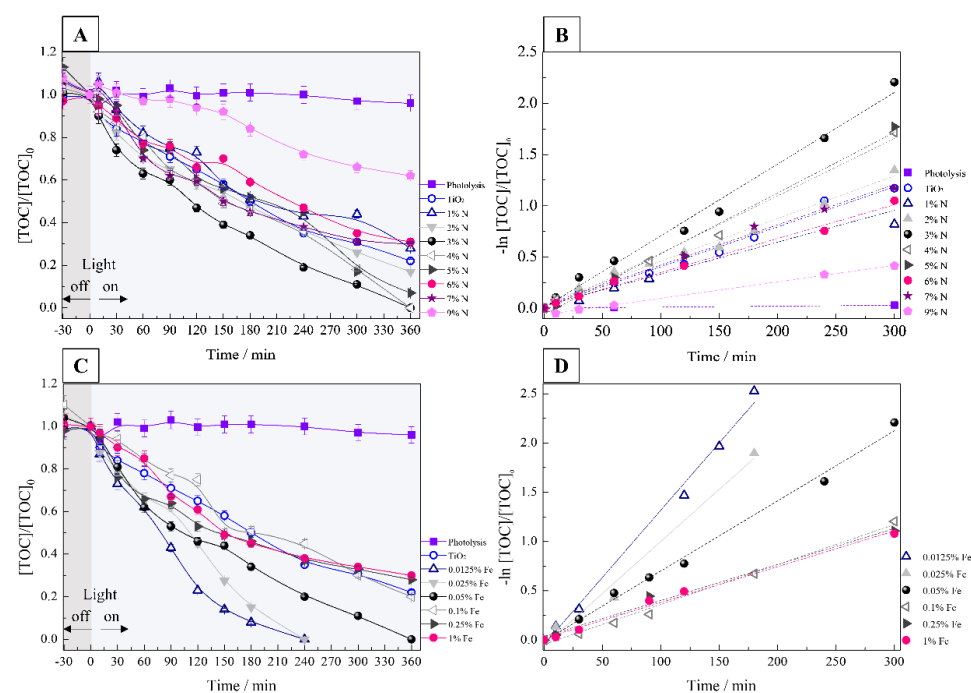


**Figure 9.** (A,C) Normalized 2,4-DMA mineralization curves obtained from the PC treatment of 350 mL of a solution of 0.1 mmol L<sup>-1</sup> of 2,4-DMA with 175 mg of photocatalyst, irradiated by a UVA lamp of 18 W (B,D) pseudo-first-order kinetics for PC treatment.

**Table 4.** Removal percentage mineralization and pseudo-first-order constant.

Photocatalysts	% Dopant ( <i>w/w</i> )	Mineralization Rate (%)		Pseudo-First-Order Constant	
		in 240 min	in 360 min	$k_{2,4\text{-DMA}}$	$R^2$
Photolysis	-	0	4	0.0001	0.961
TiO <sub>2</sub>	0	65	78	0.004	0.983
	1	57	72	0.003	0.993
TiO <sub>2</sub> + N	2	64	83	0.004	0.988
	3	81	100	0.007	0.989
	4	64	100	0.006	0.989
	5	55	93	0.006	0.983
	6	53	69	0.003	0.991
	7	62	70	0.004	0.990
	9	28	38	0.002	0.999
TiO <sub>2</sub> + Fe	0.0125	100	100	0.010	0.992
	0.025	100	100	0.010	0.980
	0.05	80	100	0.010	0.994
	0.1	55	80	0.004	0.990
	0.25	63	72	0.004	0.983
	1	62	70	0.004	0.990
TiO <sub>2</sub> + %N + 0.025 Fe	3	31	39	0.002	0.997
	4	48	52	0.002	0.992

The results also revealed that the increase above 3% of N did not improve the mineralization performance, presenting similar results to those observed for pure TiO<sub>2</sub>. The higher mineralization rate for the 3% N photocatalyst is the result of the increase in surface area (78.66 m<sup>2</sup> g<sup>-1</sup>) in relation to pure TiO<sub>2</sub> (95.69 m<sup>2</sup> g<sup>-1</sup>). It was also observed that the pore diameter was reduced from 9.72 nm (pure TiO<sub>2</sub>) to 9.03 nm (3% N), and the mean particle diameter obtained by the MET results was reduced from 16.16 nm to 12.27 nm for 3% N. With the improved contact surface, more ROS can be generated thus increasing photocatalytic activity [18,35].

Figure 9C illustrates the effect of iron content on x% Fe photocatalytic activity within 360 min reaction time. It is observed that as the doping content increases, the photocatalytic activity decreases. This decrease in photoactivity is associated with the fact that Fe<sup>3+</sup> traps both e<sup>-</sup><sub>CB</sub> and h<sup>+</sup><sub>VB</sub> up to a certain amount; as the doping content exceeds this ideal amount, it acts as a recombination center for the photogenerated charge carriers decreasing photocatalytic activity [47,52]. Thus, the 0.0125% Fe and 0.025% Fe photocatalysts mineralized 100% of 2,4-DMA in just 240 min. Furthermore, the values of  $k_{2,4\text{-DMA}}$  0.010 min<sup>-1</sup> for 0.0125% Fe and 0.025% Fe (Figure 9D, Table 4) were 2.6 times higher than mineralization with pure TiO<sub>2</sub>. In the presence of low levels of Fe doping, the charge carriers are well separated, thus increasing the efficiency of the photocatalyst. The stability of the 0.0125%Fe photocatalyst was performed and in three successive cycles, there was a reduction of only 6%. This reduction indicates good stability of the studied photocatalyst. Fe<sup>3+</sup> can serve as photogenerated hole chaser (Equation (1)). Fe<sup>4+</sup> reacts with hydroxyl ions adsorbed on the surface to produce HO• radicals (Equations (6) and (7)). Alternatively, Fe<sup>4+</sup> can also react with photogenerated electrons, improving photocatalytic activity (Equation (8)). The trapped holes would oxidize hydroxyls adsorbed on the surface to produce hydroxyl radicals [47,53].



Photocatalysts co-doped with N- and Fe- were synthesized by fixing 0.025% Fe and varying by 3 and 4% N, such amounts of N- and Fe- were selected from the photocatalytic

activities reported here. Interestingly, the junction of N- and Fe- did not show good results, as can be seen in Figure S4A (see Supplementary Material). With co-doping between N- Fe- only 50% of the 2,4-DMA was mineralized and the  $k_{2,4\text{-DMA}}$  value was two times lower than that of pure TiO<sub>2</sub> (Table 4 and Figure S4B). The increase in the surface area of the co-doped photocatalysts may have occurred, which contributed to the lack of the desired synergistic effect and to improve the photocatalytic activity. Yuan et al. reported the synthesis of N-Fe co-doped TiO<sub>2</sub> photocatalysts and tested their photocatalytic activity on 2-methylisoborneol degradation. Using a xenon lamp the highest removal efficiency was achieved when the catalyst was co-doped with 0.001% Fe and 0.5% N, with a 2-methylisoborneol removal efficiency of 99.78% in 240 min. They observed that concentrations higher than 5% of N decrease the photoactivity due to an increase in the surface area of the catalysts [54].

Table 5 shows the mineralization results of N- Fe-doped TiO<sub>2</sub> obtained in the present investigation and results of previously published studies [51–56]. For a better comparison, some parameters such as photocatalyst type, experimental conditions, model molecule for PC, light source conditions, and mineralization rate were also summarized in Table 5. In the literature, the mineralization rates found are achieved using a low volume of solution and a large amount of catalyst.

**Table 5.** Comparison of N-TiO<sub>2</sub> and Fe-TiO<sub>2</sub> photocatalysts with others.

Photocatalyst	Experimental Conditions				Model Molecule	Mineralization	Ref
	Mass/mg	Volume/mL	Light Source	Analysis Time/h			
0.0125% Fe TiO <sub>2</sub>	175	350	UV-A	4	12 ppm 2,4-DMA	100%	Present study
2 mol% Fe-TiO <sub>2</sub>	50	100	100 W fluorescent bulb	1	10 ppm Indigo Carmine	68%	[55]
N-TiO <sub>2</sub>	1	5	UV-A/solar/UV-vis	8	Microcystin-LR	80%	[56]
gC <sub>3</sub> N <sub>4</sub>	30	30	Visible-light irradiation	3	20 ppm 2,4-dichlorophenol	15.2%	[57]
BiPO <sub>4</sub> + H <sub>2</sub> O <sub>2</sub>	50	100	11 W low pressure lamp (λ = 254 nm)	2	phenol	40%	[58]
PG-C <sub>3</sub> N <sub>4</sub> /Co <sub>3</sub> O <sub>4</sub> /CoS	5	50	500 W xenon lamp	2	30 ppm Bisphenol F	51.9%	[59]
Pt <sub>SA</sub> /g-C <sub>3</sub> N <sub>4</sub>	25	100	Xenon light	4	10 ppm p-chlorophenol	70%	[60]

#### 4. Conclusions

This study provided an understanding between N- and Fe-doped photocatalysts in the mineralization of 2,4-DMA. The main results found were that:

- Nanoparticles from 16.16 to 12.27 nm were synthesized by the sol-gel method;
- The crystalline phase was exclusively anatase with a density of 3.90 g cm<sup>-3</sup>;
- The decrease in surface area from 97.70 to 78.67 m<sup>2</sup> g<sup>-1</sup> was observed to have mesopores;
- Doping with Fe at the investigated concentrations promoted substitutional positions, increasing the formation of Fe-Ti bonds. For nitrogen, there was the presence of NH<sub>3</sub>/NH<sup>4+</sup> species indicating interstitial doping;
- The 2,4-DMA mineralization was viable with high removal rates.

Therefore, our findings offer the opportunity to reconsider studies taking into account the mineralization of emerging pollutants. This avoids the use of expensive chromatographic techniques and toxicity studies as mineralization converts the pollutant into CO<sub>2</sub>, H<sub>2</sub>O, and inorganic anions.

**Supplementary Materials:** The following supporting information can be downloaded at: <https://www.mdpi.com/article/10.3390/nano12152538/s1>. Figure S1: Thermal analysis. (A) TG, and (B) DTG; Table S1: Rietveld refinement parameters for photocatalysts; Figure S2: XRD with Rietveld refinement for TiO<sub>2</sub> (A), 0.125% Fe (B) and 3% N (C); Figure S3: High-resolution XPS spectra of N 1s; Figure S4: Results for 2,4-DMA mineralization using co-doped photocatalysts fixing 0.025%Fe and varying N doping by 3 and 4%.

**Author Contributions:** Conceptualization, E.F., T.F.d.S., R.P.C. and A.M.J.; Formal analysis, E.F., T.F.d.S., P.S.C., R.F.C., D.R.V.G., S.C.d.O. and R.P.C.; Funding acquisition, A.M.J.; Investigation, E.F. and T.F.d.S.; Methodology, E.F. and T.F.d.S.; Project administration, A.M.J.; Resources, A.R.L.C. and G.A.C.; Supervision, R.P.C. and A.M.J.; Writing—original draft, T.F.d.S.; Writing—review & editing, S.C.d.O., A.R.L.C., G.A.C., R.P.C. and A.M.J. All authors have read and agreed to the published version of the manuscript.

**Funding:** This research was funded by the Brazilian funding agencies: Conselho Nacional de Desenvolvimento Científico e Tecnológico, CNPq; Coordenação de Aperfeiçoamento de Pessoal de Nível Superior, CAPES (Finance Code 001), Fundação de Amparo à Pesquisa do Estado de São Paulo, FAPESP (grant number #2019/26210-8) and Fundação de Apoio ao Desenvolvimento do Ensino, Ciência e Tecnologia do Estado de Mato Grosso do Sul, Fundect.

**Data Availability Statement:** Not applicable.

**Acknowledgments:** The authors thank MULTILAM/UFMS by SEMs analysis.

**Conflicts of Interest:** The authors declare no conflict of interest.

## References

1. Zhang, Y.; Li, H.; Tang, Y.; Luo, P.; Yang, W.; Wu, Y.; Yang, F.; Xiong, J. *Aeromonas hydrophila*-derived BioMnOx activates peroxymonosulfate for 2,4-dimethylaniline degradation in water: Mechanisms and catalyst reusability. *Process Saf. Environ. Prot.* **2022**, *158*, 308–319. [[CrossRef](#)]
2. Amat, A.M.; Arques, A.; Bossmann, S.H.; Braun, A.M.; Göb, S.; Miranda, M.A.; Oliveros, E. Oxidative degradation of 2,4-xylidine by photosensitization with 2,4,6-triphenylpyrylium: Homogeneous and heterogeneous catalysis. *Chemosphere* **2004**, *57*, 1123–1130. [[CrossRef](#)] [[PubMed](#)]
3. Jayapal, M.; Jagadeesan, H.; Krishnasamy, V.; Shanmugam, G.; Muniyappan, V.; Chidambaram, D.; Krishnamurthy, S. Demonstration of a plant-microbe integrated system for treatment of real-time textile industry wastewater. *Environ. Pollut.* **2022**, *302*, 119009. [[CrossRef](#)] [[PubMed](#)]
4. Li, J.; He, C.; Cao, X.; Sui, H.; Li, X.; He, L. Low temperature thermal desorption-chemical oxidation hybrid process for the remediation of organic contaminated model soil: A case study. *J. Contam. Hydrol.* **2021**, *243*, 103908. [[CrossRef](#)] [[PubMed](#)]
5. Machulek, A.; Gogritchiani, E.; Moraes, J.E.F.; Quina, F.H.; Braun, A.M.; Oliveros, E. Kinetic and mechanistic investigation of the ozonolysis of 2,4-xylidine (2,4-dimethyl-aniline) in acidic aqueous solution. *Sep. Purif. Technol.* **2009**, *67*, 141–148. [[CrossRef](#)]
6. Bossmann, S.H.; Wörner, M.; Pokhrel, M.R.; Baumeister, B.; Göb, S.; Braun, A.M. Ruthenium(II)-tris-bipyridine/titanium dioxide codoped zeolite Y photocatalyst: Performance optimization using 2,4-xylidine (1-amino-2,4-dimethyl-benzene). *Sep. Purif. Technol.* **2009**, *67*, 201–207. [[CrossRef](#)]
7. Zeshan, M.; Bhatti, I.A.; Mohsin, M.; Iqbal, M.; Amjed, N.; Nisar, J.; AlMasoud, N.; Alomar, T.S. Remediation of pesticides using TiO<sub>2</sub> based photocatalytic strategies: A review. *Chemosphere* **2022**, *300*, 134525. [[CrossRef](#)]
8. Friedrich, L.C.; Mendes, M.A.; Silva, V.O.; Zanta, C.L.P.S.; Machulek, A., Jr.; Quina, F.H. Mechanistic implications of zinc(II) ions on the degradation of phenol by the fenton reaction. *J. Braz. Chem. Soc.* **2012**, *23*, 1372–1377. [[CrossRef](#)]
9. Luna, A.J.; Chiavone-Filho, O.; Machulek, A.; de Moraes, J.E.F.; Nascimento, C.A.O. Photo-Fenton oxidation of phenol and organochlorides (2,4-DCP and 2,4-D) in aqueous alkaline medium with high chloride concentration. *J. Environ. Manag.* **2012**, *111*, 10–17. [[CrossRef](#)]
10. da Rosa, A.P.P.; Cavalcante, R.P.; da Silva, D.A.; da Silva, L.D.M.; da Silva, T.F.; Gozzi, F.; McGlynn, E.; Brady-Boyd, A.; Casagrande, G.A.; Wender, H.; et al. H<sub>2</sub>O<sub>2</sub>-assisted photoelectrocatalytic degradation of Mitoxantrone using CuO nanostructured films: Identification of by-products and toxicity. *Sci. Total Environ.* **2019**, *651*, 2845–2856. [[CrossRef](#)]
11. de Melo da Silva, L.; Pereira Cavalcante, R.; Fabbro Cunha, R.; Gozzi, F.; Falcao Dantas, R.; de Oliveira, S.C.; Machulek, A. Tolfenamic acid degradation by direct photolysis and the UV-ABC/H<sub>2</sub>O<sub>2</sub> process: Factorial design, kinetics, identification of intermediates, and toxicity evaluation. *Sci. Total Environ.* **2016**, *573*, 518–531. [[CrossRef](#)] [[PubMed](#)]
12. Funai, D.H.; Didier, F.; Giménez, J.; Esplugas, S.; Marco, P.; Machulek, A. Photo-Fenton treatment of valproate under UVC, UVA and simulated solar radiation. *J. Hazard. Mater.* **2017**, *323*, 537–549. [[CrossRef](#)] [[PubMed](#)]
13. Popescu, T.; Oktaviani Matei, C.; Culita, D.C.; Maraloiu, V.-A.; Rostas, A.M.; Diamandescu, L.; Iacob, N.; Savopol, T.; Ilas, M.C.; Feder, M.; et al. Facile synthesis of low toxicity iron oxide/TiO<sub>2</sub> nanocomposites with hyperthermic and photo-oxidation properties. *Sci. Rep.* **2022**, *12*, 6887. [[CrossRef](#)] [[PubMed](#)]
14. Yadav, A.A.; Hunge, Y.M.; Kang, S.W. Porous nanoplate-like tungsten trioxide/reduced graphene oxide catalyst for sonocatalytic degradation and photocatalytic hydrogen production. *Surf. Interfaces* **2021**, *24*, 101075. [[CrossRef](#)]
15. Guelfi, D.R.V.; Brillas, E.; Gozzi, F.; Machulek, A.; de Oliveira, S.C.; Sirés, I. Influence of electrolysis conditions on the treatment of herbicide bentazon using artificial UVA radiation and sunlight. Identification of oxidation products. *J. Environ. Manag.* **2019**, *231*, 213–221. [[CrossRef](#)]
16. Guelfi, D.R.V.; Gozzi, F.; Machulek, A., Jr.; Sirés, I.; Brillas, E.; de Oliveira, S.C. Degradation of herbicide S-metolachlor by electrochemical AOPs using a boron-doped diamond anode. *Catal. Today* **2018**, *313*, 182–188. [[CrossRef](#)]

17. Park, S.H.; Katoch, A.; Chae, K.H.; Gautam, S.; Miedema, P.; Cho, S.W.; Kim, M.; Wang, R.-P.; Lazemi, M.; de Groot, F.; et al. Direct and real-time observation of hole transport dynamics in anatase TiO<sub>2</sub> using X-ray free-electron laser. *Nat. Commun.* **2022**, *13*, 2531. [[CrossRef](#)]
18. Cavalcante, R.P.; Dantas, R.F.; Bayarri, B.; González, O.; Giménez, J.; Esplugas, S.; Machulek, A. Synthesis and characterization of B-doped TiO<sub>2</sub> and their performance for the degradation of metoprolol. *Catal. Today* **2015**, *252*, 27–34. [[CrossRef](#)]
19. Lee, K.M.; Lai, C.W.; Ngai, K.S.; Juan, J.C. Recent developments of zinc oxide based photocatalyst in water treatment technology: A review. *Water Res.* **2016**, *88*, 428–448. [[CrossRef](#)]
20. Venkatesan, R.; Velumani, S.; Ordon, K.; Makowska-Janusik, M.; Corbel, G.; Kassiba, A. Nanostructured bismuth vanadate (BiVO<sub>4</sub>) thin films for efficient visible light photocatalysis. *Mater. Chem. Phys.* **2018**, *205*, 325–333. [[CrossRef](#)]
21. Hunge, Y.M.; Yadav, A.A.; Kang, S.W.; Kim, H. Photocatalytic degradation of tetracycline antibiotics using hydrothermally synthesized two-dimensional molybdenum disulfide/titanium dioxide composites. *J. Colloid Interface Sci.* **2022**, *606*, 454–463. [[CrossRef](#)] [[PubMed](#)]
22. Hunge, Y.M.; Yadav, A.A.; Khan, S.; Takagi, K.; Suzuki, N.; Teshima, K.; Terashima, C.; Fujishima, A. Photocatalytic degradation of bisphenol A using titanium dioxide@nanodiamond composites under UV light illumination. *J. Colloid Interface Sci.* **2021**, *582*, 1058–1066. [[CrossRef](#)] [[PubMed](#)]
23. Ali, I.; Kim, S.-R.; Kim, S.-P.; Kim, J.-O. Anodization of bismuth doped TiO<sub>2</sub> nanotubes composite for photocatalytic degradation of phenol in visible light. *Catal. Today* **2017**, *282*, 31–37. [[CrossRef](#)]
24. Kader, S.; Al-Mamun, M.R.; Suhan, M.B.K.; Shuchi, S.B.; Islam, M.S. Enhanced photodegradation of methyl orange dye under UV irradiation using MoO<sub>3</sub> and Ag doped TiO<sub>2</sub> photocatalysts. *Environ. Technol. Innov.* **2022**, *27*, 102476. [[CrossRef](#)]
25. Bezerra, P.; Cavalcante, R.; Garcia, A.; Wender, H.; Martines, M.; Casagrande, G.; Giménez, J.; Marco, P.; Oliveira, S.; Machulek, A., Jr. Synthesis, Characterization, and Photocatalytic Activity of Pure and N-, B-, or Ag- Doped TiO<sub>2</sub>. *J. Braz. Chem. Soc.* **2017**, *28*, 1788–1802. [[CrossRef](#)]
26. Zeng, L.; Lu, Z.; Li, M.; Yang, J.; Song, W.; Zeng, D.; Xie, C. A modular calcination method to prepare modified N-doped TiO<sub>2</sub> nanoparticle with high photocatalytic activity. *Appl. Catal. B Environ.* **2016**, *183*, 308–316. [[CrossRef](#)]
27. Li, T.; Abdelhaleem, A.; Chu, W.; Pu, S.; Qi, F.; Zou, J. S-doped TiO<sub>2</sub> photocatalyst for visible LED mediated oxone activation: Kinetics and mechanism study for the photocatalytic degradation of pyrimethanil fungicide. *Chem. Eng. J.* **2021**, *411*, 128450. [[CrossRef](#)]
28. Lee, B.T.; Han, J.K.; Gain, A.K.; Lee, K.H.; Saito, F. TEM microstructure characterization of nano TiO<sub>2</sub> coated on nano ZrO<sub>2</sub> powders and their photocatalytic activity. *Mater. Lett.* **2006**, *60*, 2101–2104. [[CrossRef](#)]
29. Wafi, M.A.E.; Ahmed, M.A.; Abdel-Samad, H.S.; Medien, H.A.A. Exceptional removal of methylene blue and p-aminophenol dye over novel TiO<sub>2</sub>/RGO nanocomposites by tandem adsorption-photocatalytic processes. *Mater. Sci. Energy Technol.* **2022**, *5*, 217–231. [[CrossRef](#)]
30. Toe, E.D.; Kurniawan, W.; Mariquit, E.G.; Hinode, H. Synthesis of N-doped mesoporous TiO<sub>2</sub> by facile one-step solvothermal process for visible light photocatalytic degradation of organic pollutant. *J. Environ. Chem. Eng.* **2018**, *6*, 5125–5134. [[CrossRef](#)]
31. da Silva, A.L.; Trindade, F.J.; Dalmasso, J.L.; Ramos, B.; Teixeira, A.C.S.C.; Gouvêa, D. Synthesis of TiO<sub>2</sub> microspheres by ultrasonic spray pyrolysis and photocatalytic activity evaluation. *Ceram. Int.* **2022**, *48*, 9739–9745. [[CrossRef](#)]
32. Jadhav, P.S.; Jadhav, T.; Bhosale, M.; Jadhav, C.H.; Pawar, V.C. Structural and optical properties of N-doped TiO<sub>2</sub> nanomaterials. *Mater. Today Proc.* **2021**, *43*, 2763–2767. [[CrossRef](#)]
33. Huang, L.; Fu, W.; Fu, X.; Zong, B.; Liu, H.; Bala, H.; Wang, X.; Sun, G.; Cao, J.; Zhang, Z. Facile and large-scale preparation of N doped TiO<sub>2</sub> photocatalyst with high visible light photocatalytic activity. *Mater. Lett.* **2017**, *209*, 585–588. [[CrossRef](#)]
34. Yalçın, Y.; Kiliç, M.; Çınar, Z. Fe<sup>+3</sup>-doped TiO<sub>2</sub>: A combined experimental and computational approach to the evaluation of visible light activity. *Appl. Catal. B Environ.* **2010**, *99*, 469–477. [[CrossRef](#)]
35. da Silva, T.F.; Cavalcante, R.P.; Guelfi, D.R.V.; de Oliveira, S.C.; Casagrande, G.A.; Caires, A.R.L.; de Oliveira, F.F.; Gubiani, J.R.; Cardoso, J.C.; Machulek, A. Photo-anodes based on B-doped TiO<sub>2</sub> for photoelectrocatalytic degradation of propyphenazone: Identification of intermediates, and acute toxicity evaluation. *J. Environ. Chem. Eng.* **2022**, *10*, 107212. [[CrossRef](#)]
36. Ramos, D.D.; Bezerra, P.C.S.; Quina, F.H.; Dantas, R.F.; Casagrande, G.A.; Oliveira, S.C.; Oliveira, M.R.S.; Oliveira, L.C.S.; Ferreira, V.S.; Oliveira, S.L.; et al. Synthesis and characterization of TiO<sub>2</sub> and TiO<sub>2</sub>/Ag for use in photodegradation of methylviologen, with kinetic study by laser flash photolysis. *Environ. Sci. Pollut. Res.* **2015**, *22*, 774–783. [[CrossRef](#)]
37. Li, D.; Meng, Y.; Li, J.; Song, Y.; Xu, F. TiO<sub>2</sub>/carbonaceous nanocomposite from titanium-alginate coordination compound. *Carbohydr. Polym.* **2022**, *288*, 119400. [[CrossRef](#)]
38. Mancuso, A.; Sacco, O.; Sannino, D.; Pragliola, S.; Vaiano, V. Enhanced visible-light-driven photodegradation of Acid Orange 7 azo dye in aqueous solution using Fe-N co-doped TiO<sub>2</sub>. *Arab. J. Chem.* **2020**, *13*, 8347–8360. [[CrossRef](#)]
39. Adán, C.; Bahamonde, A.; Fernández-García, M.; Martínez-Arias, A. Structure and activity of nanosized iron-doped anatase TiO<sub>2</sub> catalysts for phenol photocatalytic degradation. *Appl. Catal. B Environ.* **2007**, *72*, 11–17. [[CrossRef](#)]
40. Khatibnezhad, H.; Ambriz-Vargas, F.; Ben Ettouil, F.; Moreau, C. Role of phase content on the photocatalytic performance of TiO<sub>2</sub> coatings deposited by suspension plasma spray. *J. Eur. Ceram. Soc.* **2022**, *42*, 2905–2920. [[CrossRef](#)]
41. Kanjana, N.; Maiaugree, W.; Poolcharuansin, P.; Laokul, P. Synthesis and characterization of Fe-doped TiO<sub>2</sub> hollow spheres for dye-sensitized solar cell applications. *Mater. Sci. Eng. B* **2021**, *271*, 115311. [[CrossRef](#)]

42. Farhangi, N.; Ayissi, S.; Charpentier, P.A. Fe doped TiO<sub>2</sub>-graphene nanostructures: Synthesis, DFT modeling and photocatalysis. *Nanotechnology* **2014**, *25*, 305601. [[CrossRef](#)] [[PubMed](#)]
43. Devi, L.G.; Kavitha, R. A review on non metal ion doped titania for the photocatalytic degradation of organic pollutants under UV/solar light: Role of photogenerated charge carrier dynamics in enhancing the activity. *Appl. Catal. B Environ.* **2013**, *140–141*, 559–587. [[CrossRef](#)]
44. He, H.; Sun, D.; Zhang, Q.; Fu, F.; Tang, Y.; Guo, J.; Shao, M.; Wang, H. Iron-Doped Cauliflower-Like Rutile TiO<sub>2</sub> with Superior Sodium Storage Properties. *ACS Appl. Mater. Interfaces* **2017**, *9*, 6093–6103. [[CrossRef](#)] [[PubMed](#)]
45. Zheng, X.; Li, Y.; You, W.; Lei, G.; Cao, Y.; Zhang, Y.; Jiang, L. Construction of Fe-doped TiO<sub>2</sub>-x ultrathin nanosheets with rich oxygen vacancies for highly efficient oxidation of H<sub>2</sub>S. *Chem. Eng. J.* **2022**, *430*, 132917. [[CrossRef](#)]
46. Chen, J.; Ding, Z.; Wang, C.; Hou, H.; Zhang, Y.; Wang, C.; Zou, G.; Ji, X. Black Anatase Titania with Ultrafast Sodium-Storage Performances Stimulated by Oxygen Vacancies. *ACS Appl. Mater. Interfaces* **2016**, *8*, 9142–9151. [[CrossRef](#)]
47. Rauf, M.A.; Meetani, M.A.; Hisaindee, S. An overview on the photocatalytic degradation of azo dyes in the presence of TiO<sub>2</sub> doped with selective transition metals. *Desalination* **2011**, *276*, 13–27. [[CrossRef](#)]
48. Liu, G.; Hua, G.Y.; Wang, X.; Cheng, L.; Pan, J.; Gao, Q.L.; Cheng, H.M. Visible light responsive nitrogen doped anatase TiO<sub>2</sub> sheets with dominant {001} facets derived from TiN. *J. Am. Chem. Soc.* **2009**, *131*, 12868–12869. [[CrossRef](#)]
49. Zhao, Y.; Zhu, L.; Yu, Y.; Gao, F.; Wang, W.; Chen, D.; Zhao, X. Facile one-pot preparation of Ti<sup>3+</sup>, N co-doping TiO<sub>2</sub> nanotube arrays and enhanced photodegradation activities by tuning tube lengths and diameters. *Catal. Today* **2020**, *355*, 563–572. [[CrossRef](#)]
50. Barkhade, T.; Banerjee, I. Optical Properties of Fe doped TiO<sub>2</sub> Nanocomposites Synthesized by Sol-Gel Technique. *Mater. Today Proc.* **2019**, *18*, 1204–1209. [[CrossRef](#)]
51. Calza, P.; Minella, M.; Demarchis, L.; Sordello, F.; Minero, C. Photocatalytic rate dependence on light absorption properties of different TiO<sub>2</sub> specimens. *Catal. Today* **2020**, *340*, 12–18. [[CrossRef](#)]
52. Moradi, V.; Ahmed, F.; Jun, M.B.G.; Blackburn, A.; Herring, R.A. Acid-treated Fe-doped TiO<sub>2</sub> as a high performance photocatalyst used for degradation of phenol under visible light irradiation. *J. Environ. Sci.* **2019**, *83*, 183–194. [[CrossRef](#)] [[PubMed](#)]
53. Ramírez-Sánchez, I.M.; Bandala, E.R. Photocatalytic Degradation of Estriol Using Iron-Doped TiO<sub>2</sub> under High and Low UV Irradiation. *Catalysts* **2018**, *8*, 625. [[CrossRef](#)]
54. Yuan, R.; Wang, S.; Liu, D.; Shao, X.; Zhou, B. Effect of the wavelength on the pathways of 2-MIB and geosmin photocatalytic oxidation in the presence of Fe-N co-doped TiO<sub>2</sub>. *Chem. Eng. J.* **2018**, *353*, 319–328. [[CrossRef](#)]
55. Sukhadeve, G.K.; Janbandhu, S.Y.; Kumar, R.; Lataye, D.H.; Ramteke, D.D.; Gedam, R.S. Visible light assisted photocatalytic degradation of Indigo Carmine dye and NO<sub>2</sub> removal by Fe doped TiO<sub>2</sub> nanoparticles. *Ceram. Int.* **2022**. [[CrossRef](#)]
56. Triantis, T.M.; Fotiou, T.; Kaloudis, T.; Kontos, A.G.; Falaras, P.; Dionysiou, D.D.; Pelaez, M.; Hiskia, A. Photocatalytic degradation and mineralization of microcystin-LR under UV-A, solar and visible light using nanostructured nitrogen doped TiO<sub>2</sub>. *J. Hazard. Mater.* **2012**, *211–212*, 196–202. [[CrossRef](#)]
57. Ma, J.; Wang, K.; Wang, C.; Chen, X.; Zhu, W.; Zhu, G.; Yao, W.; Zhu, Y. Photocatalysis-self-Fenton system with high-fluent degradation and high mineralization ability. *Appl. Catal. B Environ.* **2020**, *276*, 119150. [[CrossRef](#)]
58. Liu, Y.; Zhu, Y.; Xu, J.; Bai, X.; Zong, R.; Zhu, Y. Degradation and mineralization mechanism of phenol by BiPO<sub>4</sub> photocatalysis assisted with H<sub>2</sub>O<sub>2</sub>. *Appl. Catal. B Environ.* **2013**, *142–143*, 561–567. [[CrossRef](#)]
59. Guo, D.; Wang, Y.; Chen, C.; He, J.; Zhu, M.; Chen, J.; Zhang, C. A multi-structural carbon nitride co-modified by Co, S to dramatically enhance mineralization of Bisphenol f in the photocatalysis-PMS oxidation coupling system. *Chem. Eng. J.* **2021**, *422*, 130035. [[CrossRef](#)]
60. Zeng, Z.; Ye, F.; Deng, S.; Fang, D.; Wang, X.; Bai, Y.; Xiao, H. Accelerated organic pollutants mineralization in interlayer confined single Pt atom photocatalyst for hydrogen recovery. *Chem. Eng. J.* **2022**, *444*, 136561. [[CrossRef](#)]